Phosphorus dopants triggered single-atom platinum catalysis for efficient hydrogen evolution in proton exchange membrane electrolyzers†

Jin Peng,‡[a] Zhen Wang,‡[a] Kang Jiang,[a] Ming Peng,[a] Nithyadharseni Palaniyandy,[b] Jianwei Ren[c] and Yongwen Tan *[a]

* Corresponding authors

[a] College of Materials Science and Engineering, Hunan University, Changsha, Hunan 410082, China
E-mail: tanyw@hnu.edu.cn

[b] Institute for Catalysis and Energy Solutions (ICES), College of Science, Engineering, and Technology (CSET), University of South Africa, Florida Science Campus, Roodepoort, South Africa

[c] Department of Chemical Engineering, Faculty of Engineering, Built Environment and Information Technology, University of Pretoria, Hatfield, Pretoria, South Africa

Abstract

Proton exchange membrane water electrolyzers (PEMWE) are regarded as a prospective technique for hydrogen production due to their superior energy efficiency as well as high gas pureness. However, cost-effective and high-efficiency electrocatalysts remain to be explored to further promote their hydrogen production capacity. Herein, single-atom Pt and P atom co-doped bicontinuous nanoporous MoS_2 (Pt_{SA}, P/np-MoS_2) is constructed as an electrocatalyst for efficient hydrogen evolution reaction (HER), which exhibits outstanding electrocatalytic HER performance with a low overpotential of 24 mV at a current density of 10 mA cm^{-2}, a small Tafel slope of 28 mV dec^{-1}, and excellent long-term stability in acidic media. Experimental and theoretical investigations unambiguously uncover that the activity and stability of Pt_{SA}, P/np-MoS_2 are significantly optimized by electronic effects due to the dual-element doping, thus dramatically enhancing HER *via* thermodynamic and kinetic acceleration. More significantly, a PEMWE assembled with the prepared catalyst as a cathode demonstrates exceptional hydrogen production performance with a cell voltage of 1.67 V up to 1 A cm^{-2} as well as excellent stability.

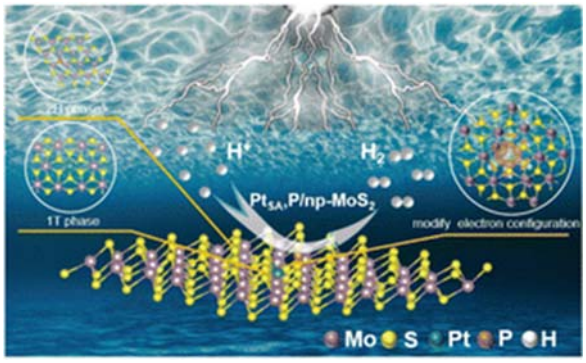

1 Introduction

Electrocatalytic water splitting driven by intermittent renewable power offers a promising and environmentally friendly strategy to generate green hydrogen with high purity.[1,2] Proton exchange membrane water electrolysis (PEMWE) is regarded as a commercially available water electrolysis technology with notable advantages, including compact structure, quick response, high efficiency, and high current density. To date, noble Pt-based metals are considered the most efficient materials to catalyze the acidic hydrogen evolution reaction (HER).[3,4] Notwithstanding that a wide array of HER electrocatalysts have been reported, inexpensive electrocatalysts with simultaneously low overpotentials and rapid reaction kinetics remain to be explored.[5,6] Therefore, in order to maximize the utilization efficiency of noble metals, the rational design and controllable synthesis of catalysts are crucial for the cost-efficient and durable HER catalytic process.[7–9]

Atomic-thickness two-dimensional materials, for instance, graphene, transition metal dichalcogenides (TMDs), and boron nitride, have drawn much attention due to their large specific surface area and unique physicochemical properties.[10,11] Among them, earth-abundant TMDs, especially molybdenum disulfide (MoS_2), are extensively utilized as HER electrocatalysts owing to their low cost and distinctive electronic structure.[12,13] Nevertheless, a significant quantity of research has proven that MoS_2, which possesses semiconducting properties, is merely catalytically active at the marginal sites, whilst the giant cardinal plane is inert, which leads to a large discount in its HER activity.[14–16] Consequently, a variety of strategies have emerged to optimize the electrocatalytic activity of MoS_2. Prevalent measures consist of phase transformations,[17] doping of heterogeneous elements,[18] and fabrication of heterojunctions.[19] Doping with heterogeneous elements (metal and nonmetal) is favored for its capability to potently regulate the electronic configuration of MoS_2, particularly the d-band centers, to render the adsorption-free energy of H* (ΔG_{H^*}) closer to thermal neutrality thus raising their HER activity.[20,21] Metal doping of MoS_2 can speed up the HER process *via* multiplying the quantity of active sites and enhancing the electroconductivity of the electrocatalyst. Nonetheless, precious metal platinum (Pt)-based electrocatalysts still display more outstanding HER activity in comparison.[22] However, the exorbitant price and rareness of Pt impede its large-scale commercialization.[23] The key to tackling this issue is to diminish the use of Pt without sacrificing its HER activity. Pt single atoms (SAs) are the crucial solution to the problem since they simultaneously lower the Pt content and expose more active sites.[24,25] Thus doping Pt SAs into a proper substrate can exert remarkable HER performance relative to other electrocatalysts at a low concentration of Pt. Although SAs doping may cause an elevation of electrocatalytic performance, it usually fails to afford simultaneously fast reaction kinetics and abundant active sites.[13] Encouragingly, recent reports have demonstrated that further doping of some non-metallic heteroatoms (such as N, P, and S) can lead to further enhancement of electrocatalytic performance by modulating the coordination environment and electronic configuration of SAs. Yin *et al.* reported that in the prepared cerium (Ce) SAs supported on a P, S, and N co-doped hollow carbon substrate, the introduction of S and P causes significant electronic modulations to the Ce SAs, promotes the electroactivity of Ce SAs and improves the overall site-to-site electron transfer, resulting in the catalyst outperforming most reported single-atom catalysts (SACs) in the oxygen reduction reaction.[26] Cao *et al.* similarly prepared a novel Si doping Fe-based SAC (Fe–N–C–Si), the results indicated that the introduction of Si would form Si–C/N bonds, which would modulate the electronic configuration of the atomic Fe sites to remarkably accelerate the crucial pathway involving *CO intermediate desorption, suppressing the poisoning of the Fe sites under high CO coverage and thus promoting the CO_2 reduction reaction performance.[27] Even though there have been

partial reports on the introduction of heteroatoms to modulate the performance of single-atom electrocatalysis, the discussion on the introduction of heteroatoms on TMDs substrates to modulate the performance of Pt SAs electrocatalytic HER is virtually untraceable. Thus, it is highly desirable to introduce nonmetallic heteroatoms to regulate the electronic structure of the single atoms supported on TMDs and deeply understand the synergetic effect, thus maximizing the HER activity of SACs.

Here, we construct metallic Pt SAs and nonmetallic P atoms co-doped bicontinuous nanoporous MoS_2 electrocatalyst (denoted as Pt_{SA}, P/np-MoS_2) for the HER under acidic conditions. The obtained nanoporous Pt_{SA}, P/np-MoS_2 electrocatalyst achieves a low overpotential of 30 mV at a current density of 10 mA cm^{-2} and a small Tafel slope of 29 mV dec^{-1} in acidic HER. Through spectroscopic characterization combined with density functional theory (DFT) calculations, we unveil that the introduction of Pt SAs can enhance the conductivity of the catalyst *via* promoting the transition of MoS_2 from the 2H phase to the 1T phase and the introduction of P atoms can modify the electron configuration surrounding Pt atoms by modulating its coordination environment, thus modulating the adsorption of hydrogen to moderate intensity to enhance the HER properties.

2 Result and discussion

2.1. Synthesis and characterizations

Fig. S1† schematically illustrates the synthesis procedure of Pt_{SA}, P/np-MoS_2 through a combination of dealloying technique, chemical vapor deposition (CVD) process, chemical etching step, and impregnation strategy. First, a self-supported nanoporous gold (NPG) substrate was obtained by selectively etching Ag in $Au_{35}Ag_{65}$ alloy through a dealloying strategy.[28,29] Then, the deposition of MoS_2 on NPG and the doping of P were accomplished *via* a two-step CVD process, respectively.[30,31] Subsequently, spontaneous reduction in the impregnation strategy and the following vacuum heating process successfully introduced isolated Pt atoms into P-doped MoS_2.[32] Finally, the NPG was removed by chemical etching in KI/I_2 solution to form the desired Pt_{SA}, P/np-MoS_2 electrocatalyst. As reflected in both scanning electron microscopy (SEM) and transmission electron microscopy (TEM) images, the prepared Pt_{SA}, P/np-MoS_2 features a three-dimensional (3D) bicontinuous nanoporous morphology, interlinked by nanotube-like structures (Fig. 1a and S2, ESI†). The average pore size of such 3D connective pore channels is estimated to be approximately 54 nm by employing the ImageJ software (Fig. S3, ESI†). The existence of these nanopores provides the catalyst with more reaction surface, accelerates the diffusion rate of the reactants, and decreases the reaction activation energy during the electrocatalytic cycle, resulting in a considerable increase in the catalytic speed. Besides, compared to Pt_{SA}, P/np-MoS_2 loaded on NPG substrate, the removal of NPG has almost no impact on the nanoporous morphology of Pt_{SA}, P/np-MoS_2 (Fig. S4, ESI†). High-resolution transmission electron microscopy (HRTEM) image illustrates the morphology of Pt_{SA}, P/np-MoS_2 from a cross-sectional perspective, from which the interlocking nanotube-like structure composed predominantly of a handful of atom-thick, atomically-bent MoS_2 can be apparently observed (Fig. 1b). High-angle annular dark-field scanning transmission electron microscopy (HAADF-STEM) image and partially magnified HAADF-STEM image present a clearer view of the lattice structure of Pt_{SA}, P/np-MoS_2, which mainly contains a massive honeycomb-like lattice of semiconducting 2H phase MoS_2 and a minority of triangular lattice of metallic 1T phase MoS_2 (Fig. 1c and d). The HAADF-STEM line intensity profile further confirms the co-existence of 2H phase MoS_2 with a sandwich-like atomic arrangement (Mo–S–Mo) and 1T phase MoS_2 with an atomic alignment of two S atoms

sandwiched between neighboring Mo atoms (Mo–S–S–Mo) (Fig. 1e). Subsequently, P atoms are verified to be doped into MoS_2 by electron energy loss spectroscopy (EELS), since two distinct regions are selected from the HAADF-STEM image for facet scan, both of which appear the L_2 and L_3 edge characteristic peak of the P atom (Fig. 1f). Similarly, the atomic resolution HAADF-STEM image demonstrates the smooth doping of Pt SAs into MoS_2, the embeddedness of Pt atoms results in the substitution of partial Mo atoms by Pt atoms, hence several scattering of atomic-level brighter dots representing Pt atoms emerge in the image due to the atomic number of Pt atom is far exceeding that of Mo atom (Fig. 1g, marked with orange circles). HAADF-STEM line intensity profile further validates the introduction of Pt single atoms and partial displacement of Mo atoms in the initial lattice (Fig. 1h). The STEM energy dispersive X-ray (EDX) spectroscopy affirms that Pt, P, Mo, and S are homogeneously distributed over the entire analyzed region (Fig. 1i).

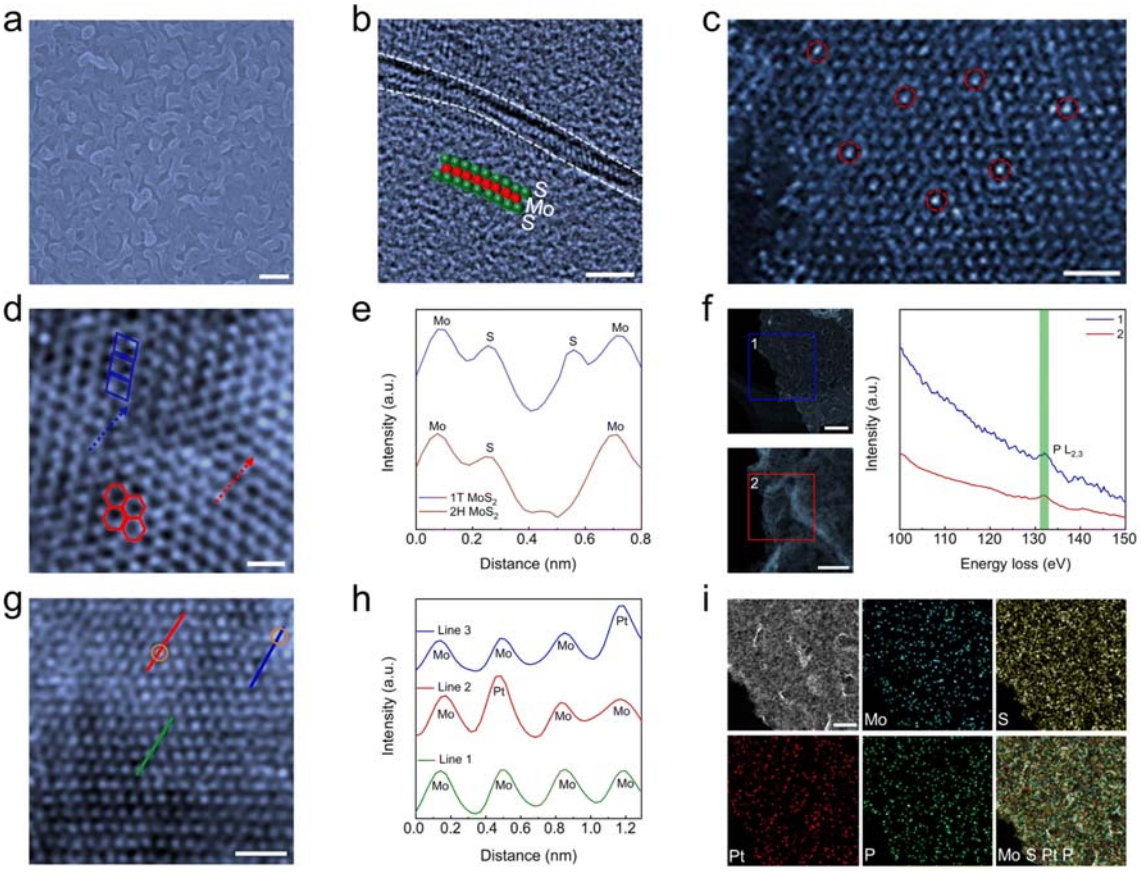

Fig. 1 Morphology and structural characterizations of Pt_{SA}, P/np-MoS_2. (a) SEM image of Pt_{SA}, P/np-MoS_2. (b) Cross-sectional HRTEM image of Pt_{SA}, P/np-MoS_2. (c) HAADF-STEM image of Pt_{SA}, P/np-MoS_2, showing the existence of isolated Pt atoms (red circles). (d) Magnified HAADF-STEM image of Pt_{SA}, P/np-MoS_2. (e) Atomic arrangement intensity profiles along two lines labeled in (d). (f) HAADF-STEM images of Pt_{SA}, P/np-MoS_2 and corresponding EELS spectra obtained at the area A and B *via* facet scan. (g) Atomic HAADF-STEM image of Pt_{SA}, P/np-MoS_2. (h) Atomic arrangement intensity profiles along three lines labeled in (g). (i) STEM-EDS elemental mapping of Pt_{SA}, P/np-MoS_2. Scale bars: (a) 200 nm, (b) 10 nm, (c) 5 nm, (d) 20 nm, (f) 200 nm (upper), 50 nm (lower), (g) 1 nm, and (i) 100 nm.

The chemical structure and phase characteristics of the Pt_{SA}, P/np-MoS_2 sample were analyzed by Raman spectroscopy. For comparison, pure nanoporous MoS_2 (denoted as np-MoS_2), the equivalent content of P-doped nanoporous MoS_2 (denoted as P/np-MoS_2), and the equivalent content of Pt SAs doped nanoporous MoS_2 (denoted as Pt_{SA}/np-MoS_2) were fabricated according to the identical method mentioned above. Fig. 2a plots the Raman spectrum of np-MoS_2, P/np-MoS_2, Pt_{SA}/np-MoS_2, and Pt_{SA}, P/np-MoS_2. Compared to np-MoS_2 and P/np-MoS_2, the appearance of several additional tiny peaks corresponding to E_{1g} (285 cm^{-1}), J_1 (149 cm^{-1}), J_2 (196 cm^{-1}), J_3 (337 cm^{-1}) vibrational modes of 1T phase MoS_2 can be recognized in Pt_{SA}/np-MoS_2 and Pt_{SA}, P/np-MoS_2.[33] Whereas the prominent peaks corresponding to in-plane (E) and out-of-plane (A_{1g}) vibrational modes of 2H phase MoS_2 exist in the vicinity of 379 cm^{-1} and 402 cm^{-1} are found in all of the above catalysts. This fully confirms the simultaneous existence of both 2H and 1T phases in Pt_{SA}/np-MoS_2 and Pt_{SA}, P/np-MoS_2, and it is revealed by comparison that it is possibly the doping of Pt SAs which displaces partial Mo atoms that facilitates this transition from the 2H phase to the 1T phase. X-ray photoelectron spectroscopy (XPS) was employed to probe the chemical state and electronic structure of the prepared Pt_{SA}, P/np-MoS_2 catalyst. The high-resolution XPS spectra of both Mo 3d orbital and S 2p orbital similarly demonstrate the co-existence of 2H and 1T phases in both Pt_{SA}/np-MoS_2 and Pt_{SA}, P/np-MoS_2. In Pt_{SA}, P/np-MoS_2 (Fig. 2b and S5, ESI†), the double peaks of XPS deconvolution of Mo 3d are attributed to 2H ($3d_{3/2}$ at 232.43 eV and $3d_{5/2}$ at 229.18 eV) and 1T ($3d_{3/2}$ at 231.60 eV and $3d_{5/2}$ at 228.21 eV) phases, and the double peaks of XPS deconvolution of S 2p are equally attributed to 2H ($2p_{1/2}$ at 163.32 eV and $2p_{3/2}$ at 162.21 eV) and 1T phases ($2p_{1/2}$ at 162.81 eV and $2p_{3/2}$ at 161.64 eV), and similar peaks can be observed in Pt_{SA}/np-MoS_2.[34] Whereas no peak corresponding to 1T phase is detected in np-MoS_2 and P/np-MoS_2, this is consistent with the outcome of the HAADF-STEM and Raman spectrum. The consequence of quantitative peak area integration of deconvolution in high-resolution XPS spectra reveals that there are approximately 85% 2H phase and 15% 1T phase in Pt_{SA}, P/np-MoS_2. Moreover, the XPS Mo 3d peak and S 2p peak of np-MoS_2, P/np-MoS_2, Pt_{SA}/np-MoS_2, and Pt_{SA}, P/np-MoS_2 are sequentially shifted toward lower binding energy, indicating the existence of robust electronic interaction between Pt atoms, P atoms, and MoS_2.[35] The high-resolution P 2p XPS spectra of Pt_{SA}, P/np-MoS_2 can be distinguished into a broader P–O peak (133.5 eV) and a narrower P–Mo peak ($2p_{1/2}$ at 130.5 eV and $2p_{3/2}$ at 129.9 eV) (Fig. 2c), implying that P atoms have successfully doped into the lattice of MoS_2 and displace a portion of S atoms,[36] whereas the occurrence of P–O bond is attributable to the unavoidable surface oxidization during the preparation of the sample.[37] Besides, the XPS P 2p peak of Pt_{SA}, P/np-MoS_2 shifts to higher binding energy compared to the XPS P 2p peak of P/np-MoS_2, similarly illustrating the interaction between P atoms and MoS_2. The high-resolution XPS Pt 4f spectra exhibit a minor positive energy shift of 0.4 eV in the XPS Pt 4f peak of Pt_{SA}, P/np-MoS_2 relative to 20% Pt/C, signifying that the Pt atoms in Pt_{SA}, P/np-MoS_2 possibly possess a positive valence state through bonding with partial S atoms in the nanoporous MoS_2, which further reinforces that Pt is probably doped into P/np-MoS_2 in the form of single atoms rather than nanoparticles,[38] it is also corroborated with the result in the HAADF-STEM spectrum (Fig. 2d). Inductively coupled plasma optical emission spectrometry (ICP-OES) result also indicates that the Pt_{SA}, P/np-MoS_2 sample contains a remarkably low content of Pt of 2.74 wt%, which is relatively close to the Pt content available from XPS (Fig. S6 and Table S1, ESI†). X-ray absorption spectroscopy (XAS) further uncovered the electronic structure and coordination environment of the Pt_{SA}, P/np-MoS_2 catalyst. Fig. 2e shows the normalized Pt L_3-edge X-ray absorption near-edge structure (XANES) spectra of Pt_{SA}/np-MoS_2, Pt_{SA}, P/np-MoS_2 as well as the references PtO_2 and Pt foil. The intensity of the white line peak of both Pt_{SA}/np-MoS_2 and Pt_{SA}, P/np-MoS_2 is between Pt foil and PtO_2, indicating that the Pt atoms therein both possess positive charges.[39] And the intensity of the white line peak of Pt_{SA}/np-MoS_2 is slightly lower than that of Pt_{SA},

P/np-MoS_2, which may be attributed to the further electron loss of Pt after the doping of P atoms. The corresponding Fourier-transformed extended X-ray absorption fine structure (FT-EXAFS) spectra in Fig. 2f unveil that both Pt_{SA}/np-MoS_2 and Pt_{SA}, P/np-MoS_2 present a main peak at ~1.90 Å and ~1.86 Å, respectively, which is smaller than ~2.48 Å at which the Pt–Pt peak occurs in Pt foil and larger than ~1.65 Å at which the Pt–O peak occurs in PtO_2, which can be assigned to the Pt–S and Pt–P/S scattering, respectively. This demonstrates the successful preparation of atomic level Pt in Pt_{SA}/np-MoS_2 and Pt_{SA}, P/np-MoS_2.[40] To elucidate the atomic dispersion and coordination environment of Pt more precisely, wavelet transform (WT) analysis was employed. As shown in Fig. 2g, the intensity maximum at ~11.5 $Å^{-1}$ which corresponds to Pt–Pt coordination is absent in both Pt_{SA}/np-MoS_2 and Pt_{SA}, P/np-MoS_2, indicating that Pt exists as single atoms. Besides, Pt_{SA}/np-MoS_2 and Pt_{SA}, P/np-MoS_2 respectively possess the intensity maximum corresponding to Pt–S and Pt–P/S coordination at ~8.4 $Å^{-1}$, signifying that Pt atoms successfully replace part of Mo atoms and coordinate with surrounding S atoms.[41] These results conform to FT-EXAFS fitting curves of Pt_{SA}, P/np-MoS_2 catalyst (Fig. S8b and Table S2, ESI†). Fig. S7a† presents the Mo K-edge XANES spectra of np-MoS_2, P/np-MoS_2, Pt_{SA}/np-MoS_2, and Pt_{SA}, P/np-MoS_2 along with Mo foil as a reference. The enlarged Mo K near-edge absorption energy spectra (inset in Fig. S7a†) show that the near-edge absorption energy of np-MoS_2, P/np-MoS_2, Pt_{SA}/np-MoS_2, and Pt_{SA}, P/np-MoS_2, and Mo foil declines in sequence, which demonstrates that the valence state of Mo in Pt_{SA}, P/np-MoS_2 is located between 0 and +4, and the doping of both Pt SAs and P atoms will lead to the movement of Mo valence state to more negative values, in agreement with the XPS results.[42] The corresponding FT-EXAFS spectra in Fig. S7b† unveil the presence of two peaks located at ~1.91 Å and ~2.92 Å attributed to the Mo–S and Mo–Mo scattering paths in both np-MoS_2, P/np-MoS_2, Pt_{SA}/np-MoS_2, and Pt_{SA}, P/np-MoS_2. However, a minor peak located at ~2.42 Å is discovered just in P/np-MoS_2 and Pt_{SA}, P/np-MoS_2, which probably results from the coordination between the Mo atoms and P atoms.[43] This result conforms to FT-EXAFS fitting curves of Pt_{SA}, P/np-MoS_2 catalyst (Fig. S8a and Table S2, ESI†). These hints that P atoms doping is likely to substitute parts of the S atoms in MoS_2 and thereafter form chemical bonds with surrounding Mo atoms, which is consistent with the results obtained by XPS. Furthermore, the WT-EXAFS spectra in Fig. S9† similarly validate the existence of an intensity maximum at ~10.5 $Å^{-1}$ in *k* space which is assigned to Mo–P scattering in Pt_{SA}, P/np-MoS_2.[44] S K-edge XANES spectra exhibit a drop in the white line resonance strength of Pt_{SA}, P/np-MoS_2 relative to np-MoS_2, which ascribes probably to the transition of the 2H phase to the 1T phase as a consequence of the co-doping of Pt SAs and P atoms, which also corroborates with the conclusions drawn previously (Fig. S10, ESI†).[32]

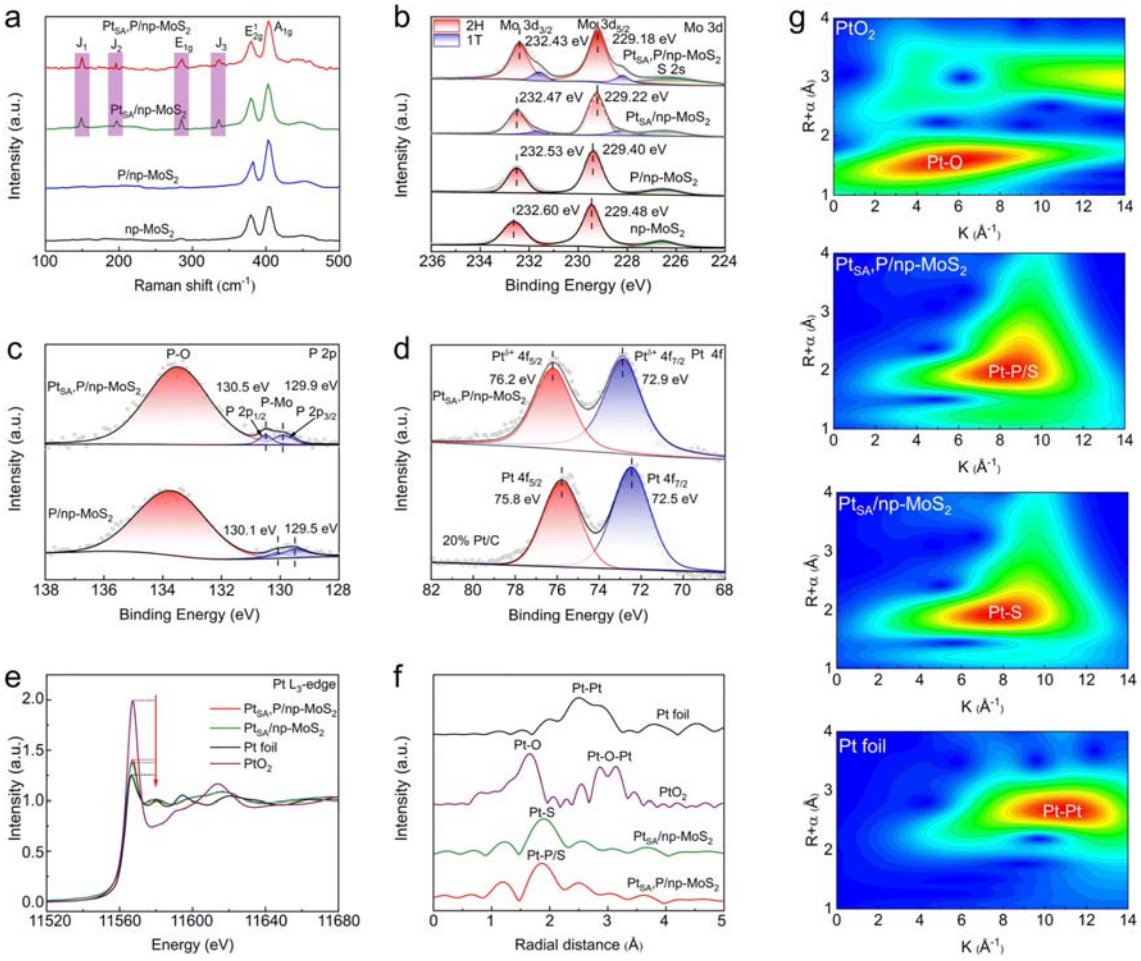

Fig. 2 Electronic state and atomic structure characterization analyses. (a) Raman spectra of np-MoS_2, P/np-MoS_2, Pt_{SA}/np-MoS_2, and Pt_{SA}, P/np-MoS_2. (b–d) High-resolution XPS spectra of (b) Mo 3d, (c) P 2p, and (d) Pt 4f. (e) Pt L_3-edge XANES spectra of Pt_{SA}/np-MoS_2, Pt_{SA}, P/np-MoS_2, PtO_2, and Pt foil. (f) Corresponding FT-EXAFS spectra from (e). (g) Wavelet transforms of PtO_2, Pt foil, Pt_{SA}/np-MoS_2, and Pt_{SA}, P/np-MoS_2.

2.2. Electrochemical HER performance

The electrochemical HER performance of all the above-mentioned catalysts including Pt_{SA}, P/np-MoS_2 as well as the commercial Pt/C catalyst as a reference was measured utilizing a conventional three-electrode system in Ar-saturated 0.5 M H_2SO_4 electrolyte at room temperature. Fig. 3a illustrates the linear sweep voltammetry (LSV) curves corrected through *iR* at a scan rate of 5 mV s^{-1}. Apparently, the simultaneous introduction of Pt SAs and P atoms can drastically boost the HER performance of Pt_{SA}, P/np-MoS_2. Amidst all the catalysts, Pt_{SA}, P/np-MoS_2 presents the most outstanding HER performance with a remarkably low overpotential of 24 mV at a current density of 10 mA cm^{-2}. This value is considerably smaller than that of np-MoS_2 (273 mV), P/np-MoS_2 (162 mV), Pt_{SA}/np-MoS_2 (74 mV), and commercial Pt/C (20 wt%) (30 mV). Specifically, Pt_{SA}, P/np-MoS_2 possesses a high mass activity of 5.97 A mg_{Pt}^{-1} which is 10.3 times and 24.9 times larger than that of the commercial Pt/C (0.58 A mg_{Pt}^{-1}) and Pt_{SA}/np-MoS_2 (0.24 mA mg_{Pt}^{-1}), respectively, proving its cost-effectiveness in the application (Fig. 3b). The Tafel plots in Fig. 3c have also been employed to estimate the catalytic activity of the above catalysts. Pt_{SA}, P/np-MoS_2 manifests the minimum Tafel slope

of 28 mV dec^{-1}, which is notably lower than those of np-MoS_2 (162 mV dec^{-1}), P/np-MoS_2 (74 mV dec^{-1}), Pt_{SA}/np-MoS_2 (41 mV dec^{-1}), and commercial Pt/C (20 wt%) (29 mV dec^{-1}). This implies that Pt_{SA}, P/np-MoS_2, similarly to commercial Pt/C, exhibits superior reaction kinetics *via* the Volmer–Tafel mechanism compared to np-MoS_2, P/np-MoS_2, and Pt_{SA}/np-MoS_2*via* the Volmer–Heyrovsky mechanism. In addition, when the scan rate was reduced from 5 mV s^{-1} to 1 mV s^{-1}, the HER performance of Pt_{SA}, P/np-MoS_2 was slightly reduced, and the Tafel slope obtained from it increased by only 0.3 mV dec^{-1} (Fig. S11, ESI†). Furthermore, based on the whole comparison of overpotentials at 10 mA cm^{-2} and Tafel slopes for Pt_{SA}, P/np-MoS_2 with those reported TMDs-based electrocatalysts, it can be observed that Pt_{SA}, P/np-MoS_2 demonstrates the best HER performance among Pd, Re–MoS_2,[45] Cu–Pd–MoS_2,[46] Pt@MoS_2 (ref. 47) and so on (Fig. 3d and Table S3, ESI†). The electrochemical impedance spectroscopy (EIS) indicates that Pt_{SA}, P/np-MoS_2 owns the lowest value of charge transfer resistance (R_{ct}) relative to np-MoS_2, P/np-MoS_2, and Pt_{SA}/np-MoS_2, thus enabling an enhancement of the interfacial electron transfer kinetics (Fig. 3e). The electrochemical surface area (ECSA) of catalysts was assessed by the double-layer capacitance (C_{dl}) acquired from the relevant cyclic voltammetry (CV) curves in the non-faradaic potential region at varied scan rates. By calculation, Pt_{SA}, P/np-MoS_2 displays the maximum C_{dl} value of 70.5 mF cm^{-2} among all catalysts, which is 1.1 times higher than Pt_{SA}/np-MoS_2 (65 mF cm^{-2}), 2 times higher than P/np-MoS_2 (35.5 mF cm^{-2}) and 3 times higher than np-MoS_2 (23.5 mF cm^{-2}), respectively (Fig. S12, ESI†). Moreover, among them, Pt_{SA}, P/np-MoS_2 possesses the most outstanding HER performance simultaneously with the largest ECSA calculated by C_{dl}, revealing that the incorporation of Pt SAs and P atoms will enlarge the electrochemically active area hence entailing the exposure of more active sites (Fig. S13, ESI†). The faradaic efficiency of Pt_{SA}, P/np-MoS_2 for H_2 production in 1 h is well maintained at ~100%, which indicates that there is almost no other reduction product (Fig. S14, ESI†). Besides, Pt_{SA}, P/np-MoS_2 exhibits long-term stability at a current density of 10 mA cm^{-2} over 100 h as well as negligible current density loss after 1000 cycles of CV (Fig. 3f). Moreover, the SEM, TEM, Raman, and XPS spectra of Pt_{SA}, P/np-MoS_2 show no obvious change after 100 hours of cyclic stability test (Fig. S15–S17, ESI†). Simultaneously, Pt_{SA}, P/np-MoS_2 can maintain uniformly dispersed Pt SAs without aggregation after 100 hours of cyclic stability test (Fig. S18, ESI†).

The extraordinary HER performance and outstanding stability of Pt_{SA}, P/np-MoS_2 catalyst prompted us to further investigate its property in proton exchange membrane water electrolyzers (PEMWE), which simulate industrial production conditions. The PEMWE for overall water electrolysis was assembled with Pt_{SA}, P/np-MoS_2 as the cathode catalyst, commercial IrO_2 as the anode catalyst, Ar-saturated 0.5 M H_2SO_4 solution as the electrolyte, and Nafion 117 as the proton exchange membrane (PEM) (Fig. 4a). In Fig. 4b, polarization curves measured at 60 °C demonstrate that IrO_2‖Pt_{SA}, P/np-MoS_2 electrolyte with a cell voltage of 1.67 V up to 1 A cm^{-2} and 1.89 V up to 2 A cm^{-2} has superior behavior in comparison to IrO_2‖Pt/C (20 wt%) electrolyte with a cell voltage of 1.71 V up to 1 A cm^{-2} and 1.96 V up to 2 A cm^{-2}, respectively. Moreover, Pt_{SA}, P/np-MoS_2 possesses a smaller cell voltage at a current density of 1 A cm^{-2}, outperforms a majority of reported TMDs-based catalysts including defect-rich MoS_2/CFP,[48] M–$CoSe_{1.28}S_{0.72}$,[49] FeMoS/C,[50] Mo_3S_{13}/CB,[51] and Mo_3S_{13}/NCNT[52] (Fig. 4c). Furthermore, the IrO_2‖Pt_{SA}, P/np-MoS_2 electrolyzer presents a negligible cell voltage value variation at a current density of 1 A cm^{-2} over 130 h (Fig. 4d).

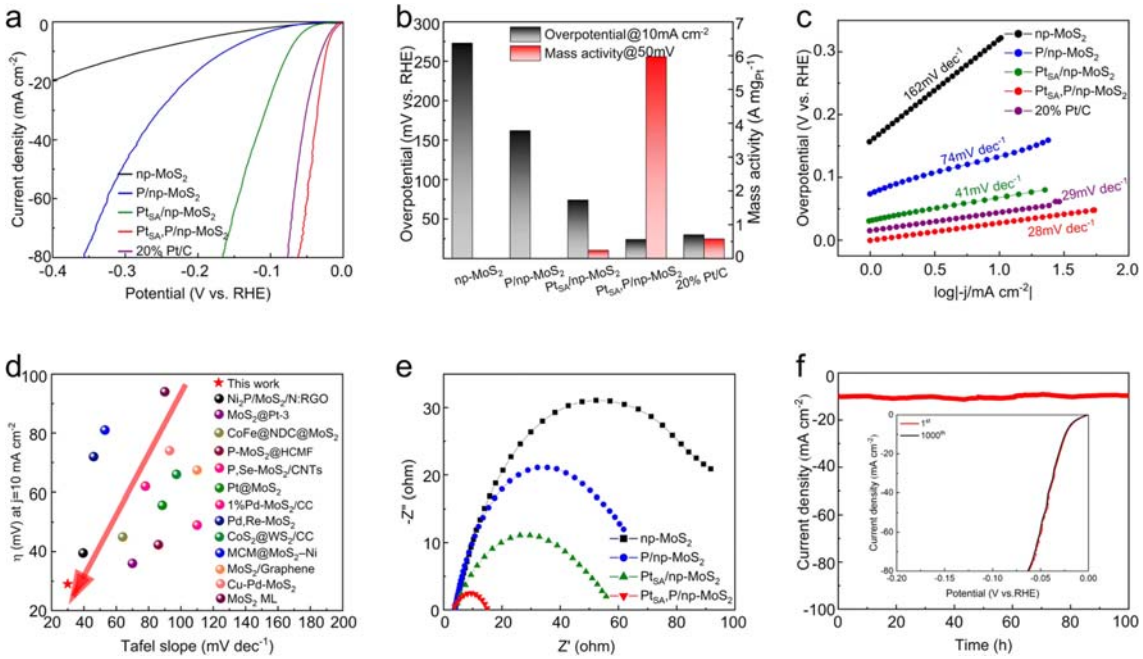

Fig. 3 Electrochemical HER performance in 0.5 M H_2SO_4. (a) HER polarization curves of np-MoS_2, P/np-MoS_2, Pt_{SA}/np-MoS_2, Pt_{SA}, P/np-MoS_2, and commercial Pt/C (20 wt%). (b) The overpotential column at a current density of 10 mA cm^{-2} derived from (a) and the Pt mass activity column at the overpotential of 50 mV. (c) Corresponding Tafel plots derived from (a). (d) Comparison of overpotential (η) at a current density of 10 mA cm^{-2} and Tafel slope of Pt_{SA}, P/np-MoS_2 with reported TMDs-based HER catalysts in 0.5 M H_2SO_4 solution. Values were plotted from references (Table S3, ESI†). (e) EIS Nyquist plots of np-MoS_2, P/np-MoS_2, Pt_{SA}/np-MoS_2, and Pt_{SA}, P/np-MoS_2. (f) Chronopotentiometry curve of the Pt_{SA}, P/np-MoS_2 catalyst at a current density of 10 mA cm^{-2} for 100 h. The inset presents the initial and 1000th polarization curves of the Pt_{SA}, P/np-MoS_2 catalyst.

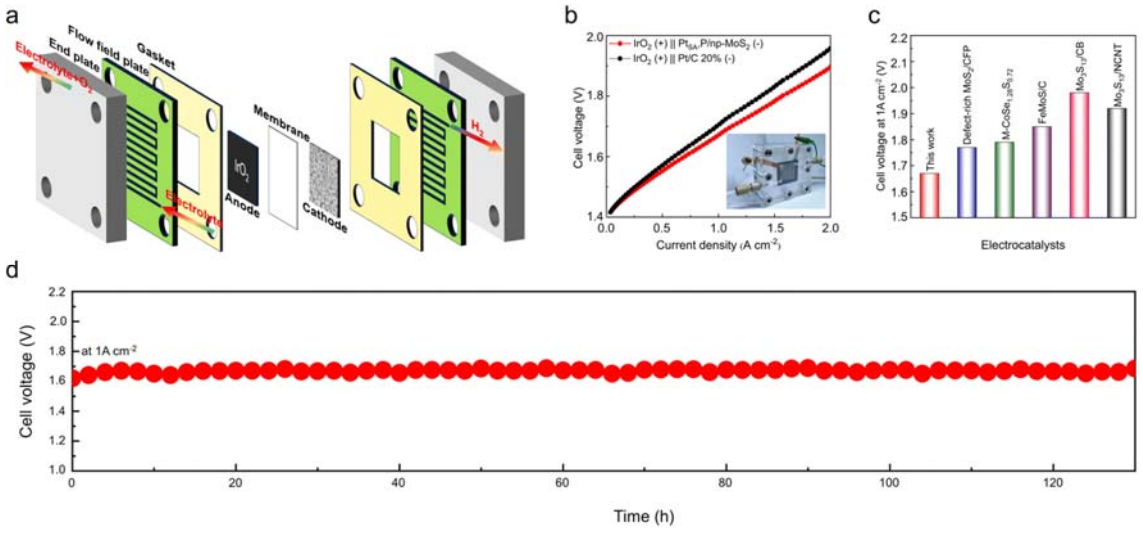

Fig. 4 PEMWE performance in 0.5 M H_2SO_4. (a) The schematic diagram of PEMWE. (b) Polarization curves for overall water splitting of IrO_2‖Pt_{SA}, P/np-MoS_2 and IrO_2‖Pt/C (20 wt%). The inset presents the optical photograph of the PEMWE. (c) Comparison of the cell voltage at 1 A cm^{-2} between Pt_{SA}, P/np-MoS_2 and other TMDs-based electrocatalysts reported in the literature. (d) Chronopotentiometry curve at 1 A cm^{-2} for overall water splitting of IrO_2‖Pt_{SA}, P/np-MoS_2.

2.3. DFT calculations

DFT calculations were implemented to further explore how Pt SAs and P atoms act synergistically on nanoporous MoS_2 to enhance the HER performance. We constructed seven optimized atomic configurations for comparison, which are np-MoS_2 (2H-MoS_2), 1T-MoS_2, P/np-MoS_2 (P/2H-MoS_2), 2H phase in Pt_{SA}/np-MoS_2 (Pt_{SA}/2H-MoS_2), 1T phase in Pt_{SA}/np-MoS_2 (Pt_{SA}/1T-MoS_2), 2H phase in Pt_{SA}, P/np-MoS_2 (Pt_{SA}, P/2H-MoS_2), 1T phase in Pt_{SA}, P/np-MoS_2 (Pt_{SA}, P/1T-MoS_2). Among them, the replacement of Mo and S atoms by Pt and P atoms in Pt_{SA}, P/np-MoS_2, respectively, is also consistent with the above experimental results (Fig. S19, ESI†). Fig. S20† illustrates the corresponding optimized atomic configurations for the adsorption state of H protons (H*). It can be observed that H* is mainly adsorbed at the S site without the introduction of Pt and P atoms, and when Pt and P atoms are introduced, it is predominantly adsorbed at the P site neighboring the Pt atom. Fig. S21† presents the total density of states (TDOS) map of the above optimized atomic configurations, it is noteworthy that 2H-MoS_2 possesses comparatively poor conductivity due to its large band gap,[53] whereas Pt SA doping is beneficial to induce the transition from 2H MoS_2 to 1T MoS_2, leading to a decrease in the band gap and an increase in the number of new gap states crossing the Fermi energy (E_F) level, enhancing the overall conductivity, thus facilitating the charge transfer in the HER process and improving the HER performance, which is also concordant with the EIS results. Moreover, the charge density difference profiles reveal that the introduction of P atoms in Pt_{SA}, P/np-MoS_2 drastically modulates the electronic states around the Pt atoms, resulting in the transfer of electrons from the Pt atoms to the surrounding P and S atoms (Fig. 5a and b), thereby accelerating the HER catalytic reaction. Fig. 5c shows the projected density of states (PDOS) of Pt_{SA}/1T-MoS_2 and Pt_{SA}, P/1T-MoS_2 before and after the adsorption of H. Similarly, it is observable that following the introduction of P atoms, Pt_{SA}, P/1T-MoS_2 will induce the generation of a new empty $3p_x$ orbital above the E_F level, which will benefit in regulating the adsorption strength of H and hence strengthen the HER performance. In investigating the catalytic performance of HER, the ΔG_{H^*} on the catalyst surface is generally a crucial parameter, where the desired catalyst should provide a value of ΔG_{H^*} close to zero.[54] As demonstrated in Fig. 5d, 2H-MoS_2 exhibits a large positive ΔG_{H^*} value of 1.88 eV, indicating that the adsorption ability of H on the surface of the catalyst is extremely weak, which will lead to the difficulty for reactants to be adsorbed on its surface. However, after the introduction of P atoms, P/MoS_2 shows a remarkably large negative ΔG_{H^*} value of −1.01 eV, demonstrating that the adsorption capacity of H on its surface is excessively strong, which will result in the hardship of subsequent H_2 production to be desorbed from its surface. Both situations will hinder the smooth progress of the HER process. With the further introduction of Pt SAs, Pt_{SA}, P/MoS_2 possesses a negative ΔG_{H^*} value closest to 0 eV, which signifies that the adsorption of H on its surface is moderately intensive, which will enable the whole reaction to reach the fastest reaction rate and significantly promote the HER process. All the above calculations confirm that the co-doping of Pt SAs and P atoms into nanoporous MoS_2 will respectively optimize the overall conductivity of the catalyst and moderate the adsorption strength of H thereby improving the HER behavior of Pt_{SA}, P/np-MoS_2.

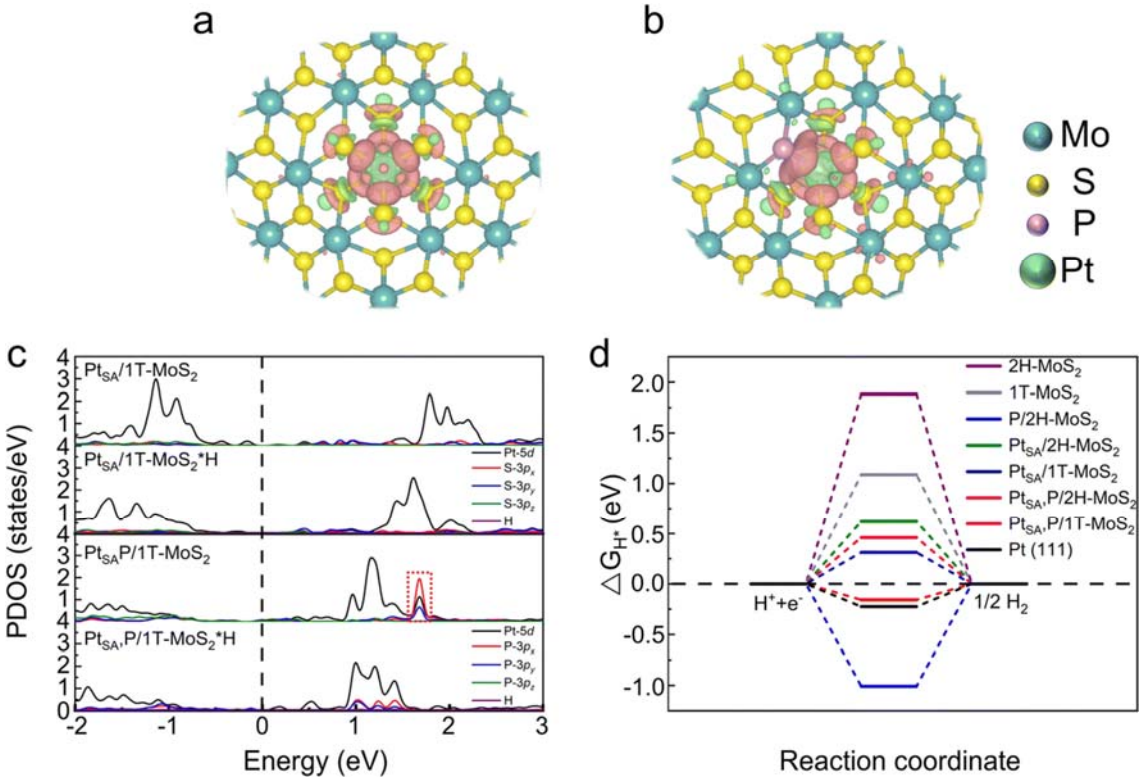

Fig. 5 DFT calculations. Top view of charge density difference for (a) Pt_{SA}/1T-MoS_2 and (b) Pt_{SA}, P/1T-MoS_2. (c) PDOS of Pt_{SA}/1T-MoS_2 and Pt_{SA}, P/1T-MoS_2 before and after the adsorption of H. (d) The calculated Gibbs hydrogen adsorption free energy (ΔG_{H^*}) plot of the 2H-MoS_2, 1T-MoS_2, P/2H-MoS_2, Pt_{SA}/2H-MoS_2, Pt_{SA}/1T-MoS_2, Pt_{SA}, P/2H-MoS_2, Pt_{SA}, P/1T-MoS_2.

3 Conclusion

In summary, we demonstrated that the simultaneous injection of atomic Pt and P species triggers nanoporous MoS_2 toward highly active and long-term stable HER. Spectroscopic measurements and DFT calculations unveil that the injection of Pt SAs into the lattice of nanoporous MoS_2 can induce more phase conversion from 2H to metallic 1T, thus increasing the metallic characteristics of MoS_2, while the injection of P atoms into the lattice of nanoporous MoS_2 can modulate the electron configuration surrounding Pt atoms by modifying its coordination environment, thereby strengthening the interaction between Pt atoms and the reaction intermediates. As a result, the Pt_{SA}, P/np-MoS_2 shows high HER activity with a low overpotential of 24 mV at a current density of 10 mA cm^{-2} and a low Tafel slope of 28 mV dec^{-1}, along with superior operating durability. More importantly, a PEM electrolyzer assembled with this catalyst as a cathode can be stably operated at 1 A cm^{-2} for over 140 hours, suggesting its potential for industrial applications. This work not only provides a synergistic doping strategy to attain high activity and outstanding stability of nanoporous MoS_2 but also enlightens the rational design of more effective electrocatalysts for renewable energy development.

Data availability

The data supporting this article have been included as part of the ESI.†

Author contributions

Jin Peng: investigation, conceptualization, methodology, data curation, formal analysis, visualization, writing – original draft. Zhen Wang: formal analysis, data curation, visualization, DFT calculation, validation, writing – review and editing. Kang Jiang: methodology, data curation, formal analysis. Ming Peng: supervision, resources, funding acquisition. Nithyadharseni Palaniyandy: resources, supervision. Jianwei Ren: resources, supervision. Yongwen Tan: conceptualization, methodology, formal analysis, funding acquisition, supervision, project administration, resources, writing – review and editing.

Conflicts of interest

There are no conflicts to declare.

Acknowledgements

The authors greatly appreciate the financial support from the National Key R&D Program of China (no. 2021YFA1500900), the National Natural Science Foundation of China (no. 52371221, U23A20554), the Natural Science Foundation of Hunan Province (no. 2022JJ30005), and the Fundamental Research Funds for the Central Universities.

Notes and references

1. R. Daw , J. Finkelstein and M. Helmer , *Nature*, 2012, **488** , 293.
2. S. Ott *Science*, 2011, **333** , 1714 —1715 .
3. S. Liu , Y. Shen , Y. Zhang , B. Cui , S. Xi , J. Zhang , L. Xu , S. Zhu , Y. Chen , Y. Deng and W. Hu , *Adv. Mater.*, 2022, **34** , 2106973 .
4. J. Zhu , L. Hu , P. Zhao , L. Y. S. Lee and K.-Y. Wong , *Chem. Rev.*, 2019, **120** , 851 —918 .
5. C. Lei , Y. Wang , Y. Hou , P. Liu , J. Yang , T. Zhang , X. Zhuang , M. Chen , B. Yang , L. Lei , C. Yuan , M. Qiu and X. Feng , *Energy Environ. Sci.*, 2019, **12** , 149 —156 .
6. Y. Huang , J. Ge , J. Hu , J. Zhang , J. Hao and Y. Wei , *Adv. Energy Mater.*, 2018, **8** , 1701601 .
7. K. Cheng , L. C. J. Smulders , L. I. van der Wal , J. Oenema , J. D. Meeldijk , N. L. Visser , G. Sunley , T. Roberts , Z. Xu , E. Doskocil , H. Yoshida , Y. Zheng , J. Zečević , P. E. de Jongh and K. P. de Jong , *Science*, 2022, **377** , 204 —208 .
8. Z. Li , J. Y. Fu , Y. Feng , C. K. Dong , H. Liu and X. W. Du , *Nat. Catal.*, 2019, **2** , 1107 —1114 .
9. J. Li , M. Yan , X. Zhou , Z.-Q. Huang , Z. Xia , C.-R. Chang , Y. Ma and Y. Qu , *Adv. Funct. Mater.*, 2016, **26** , 6785 —6796 .
10. H. Tao , Q. Fan , T. Ma , S. Liu , H. Gysling , J. Texter , F. Guo and Z. Sun , *Prog. Mater. Sci.*, 2020, **111** , 100637
11. J. Zhang , J. Wu , X. Zou , K. Hackenberg , W. Zhou , W. Chen , J. Yuan , K. Keyshar , G. Gupta , A. Mohite , P. M. Ajayan and J. Lou , *Mater. Today*, 2019, **25** , 28 —34 .
12. A. Mondal and A. Vomiero , *Adv. Funct. Mater.*, 2022, **32** , 2208994 .
13. J. Zhang , T. Wang , P. Liu , S. H. Liu , R. H. Dong , X. D. Zhuang , M. W. Chen and X. L. Feng , *Energy Environ. Sci.*, 2016, **9** , 2789 —2793 .
14. J. Kibsgaard , Z. B. Chen , B. N. Reinecke and T. F. Jaramillo , *Nat. Mater.*, 2012, **11** , 963 —969 .

15. Z. Y. Luo , Y. X. Ouyang , H. Zhang , M. L. Xiao , J. J. Ge , Z. Jiang , J. L. Wang , D. M. Tang , X. Z. Cao , C. P. Liu and W. Xing , *Nat. Commun.*, 2018, **9** , 2120 .
16. X. Y. Shi , S. Posysaev , M. Huttula , V. Pankratov , J. Hoszowska , J. C. Dousse , F. Zeeshan , Y. R. Niu , A. Zakharov , T. H. Li , O. Miroshnichenko , M. Zhang , X. Wang , Z. J. Huang , S. Saukko , D. L. González , S. van Dijken , M. Alatalo and W. Cao , *Small*, 2018, **14** , 1704526
17. B. Gao , Y. Zhao , X. Du , Y. Chen , B. Guan , Y. Li , Y. Li , S. Ding , H. Zhao , C. Xiao and Z. Song , *J. Mater. Chem. A*, 2021, **9** , 8394 —8400
18. Q. Z. Xiong , Y. Wang , P. F. Liu , L. R. Zheng , G. Z. Wang , H. G. Yang , P. K. Wong , H. M. Zhang and H. J. Zhao , *Adv. Mater.*, 2018, **30** , 1801450 .
19. K. R. G. Lim , A. D. Handoko , L. R. Johnson , X. Meng , M. Lin , G. S. Subramanian , B. Anasori , Y. Gogotsi , A. Vojvodic and Z. W. Seh , *ACS Nano*, 2020, **14** , 16140 —16155 .
20. Q. Fu , J. Han , X. Wang , P. Xu , T. Yao , J. Zhong , W. Zhong , S. Liu , T. Gao , Z. Zhang , L. Xu and B. Song , *Adv. Mater.*, 2021, **33** , 1907818 .
21. D. Voiry , J. Yang and M. Chhowalla , *Adv. Mater.*, 2016, **28** , 6197 —6206
22. X. Zhao , M. Zheng , Z. Zhang , Y. Wang , Y. Zhou , X. Zhou and H. Zhang , *J. Mater. Chem. A*, 2021, **9** , 16427 —16435 .
23. J. Guo , J. Liu , X. Zhang , X. Guan , M. Zeng , J. Shen , J. Zou , Q. Chen , T. Wang and D. Qian , *J. Mater. Chem. A*, 2022, **10** , 13727 —13734 .
24. J. Zhu , Y. Tu , L. Cai , H. Ma , Y. Chai , L. Zhang and W. Zhang , *Small*, 2022, **18** , 2104824 .
25. F. Y. Yu , Z. L. Lang , Y. J. Zhou , K. Feng , H. Q. Tan , J. Zhong , S. T. Lee , Z. H. Kang and Y. G. Li , *ACS Energy Lett.*, 2021, **6** , 4055 —4062 .
26. L. Yin , S. Zhang , M. Sun , S. Wang , B. Huang and Y. Du , *Adv. Mater.*, 2023, **35** , 2302485 .
27. C. Cao , S. Zhou , S. Zuo , H. Zhang , B. Chen , J. Huang , X.-T. Wu , Q. Xu and Q.-L. Zhu , *Research*, 2023, **6** , 0079 .
28. Y. Tan , P. Liu , L. Chen , W. Cong , Y. Ito , J. Han , X. Guo , Z. Tang , T. Fujita , A. Hirata and M. W. Chen , *Adv. Mater.*, 2014, **26** , 8023 —8028 .
29. D. Chen , Z. Wei , M. Wang , S. Zhao , P. Liu , A. Pan and Y. Tan , *Nano Lett.*, 2022, **22** , 7020 —7027 .
30. A. Shivayogimath , J. D. Thomsen , D. M. A. Mackenzie , M. Geisler , R.-M. Stan , A. J. Holt , M. Bianchi , A. Crovetto , P. R. Whelan , A. Carvalho , A. H. C. Neto , P. Hofmann , N. Stenger , P. Bøggild and T. J. Booth , *Nat. Commun.*, 2019, **10** , 2957 .
31. D. Chen , S. Ning , J. Lan , M. Peng , H. Duan , A. Pan and Y. Tan , *Adv. Mater.*, 2020, **32** , 2004055 .
32. K. Jiang , M. Luo , Z. Liu , M. Peng , D. Chen , Y.-R. Lu , T.-S. Chan , F. M. F. de Groot and Y. Tan , *Nat. Commun.*, 2021, **12** , 1687 .
33. R. Liu , T. Guo , H. Fei , Z. Wu , D. Wang and F. Liu , *Adv. Sci.*, 2022, **9** , 2103583
34. K. Qi , X. Cui , L. Gu , S. Yu , X. Fan , M. Luo , S. Xu , N. Li , L. Zheng , Q. Zhang , J. Ma , Y. Gong , F. Lv , K. Wang , H. Huang , W. Zhang , S. Guo , W. Zheng and P. Liu , *Nat. Commun.*, 2019, **10** , 5231 .
35. A. Shan , X. Teng , Y. Zhang , P. Zhang , Y. Xu , C. Liu , H. Li , H. Ye and R. Wang , *Nano Energy*, 2022, **94** , 106913 .
36. J. Xu , X. Yan , Y. Qi , Y. Fu , C. Wang and L. Wang , *Chem. Eng. J.*, 2019, **375** , 122053 .
37. W. Wang , Y. Song , C. Ke , Y. Li , Y. Liu , C. Ma , Z. Wu , J. Qi , K. Bao , L. Wang , J. Wu , S. Jiang , J. Zhao , C.-S. Lee , Y. Chen , G. Luo , Q. He and R. Ye , *ACS Nano*, 2023, **17** , 1287 —1297 .

38. H. Zhang , P. An , W. Zhou , B. Y. Guan , P. Zhang , J. Dong and X. W. Lou , *Sci. Adv.*, 2018, **4** , eaao6657 .
39. S. Tian , B. Wang , W. Gong , Z. He , Q. Xu , W. Chen , Q. Zhang , Y. Zhu , J. Yang , Q. Fu , C. Chen , Y. Bu , L. Gu , X. Sun , H. Zhao , D. Wang and Y. Li , *Nat. Commun.*, 2021, **12** , 3181 .
40. Z. Shi , X. Zhang , X. Lin , G. Liu , C. Ling , S. Xi , B. Chen , Y. Ge , C. Tan , Z. Lai , Z. Huang , X. Ruan , L. Zhai , L. Li , Z. Li , X. Wang , G.-H. Nam , J. Liu , Q. He , Z. Guan , J. Wang , C.-S. Lee , A. R. J. Kucernak and H. Zhang , *Nature*, 2023, **621** , 300 —305 .
41. K. L. Zhou , Z. Wang , C. B. Han , X. Ke , C. Wang , Y. Jin , Q. Zhang , J. Liu , H. Wang and H. Yan , *Nat. Commun.*, 2021, **12** , 3783 .
42. Y. Sun , Y. Zang , W. Tian , X. Yu , J. Qi , L. Chen , X. Liu and H. Qiu , *Energy Environ. Sci.*, 2022, **15** , 1201 —1210 .
43. M. S. Duyar , A. Gallo , S. K. Regli , J. L. Snider , J. A. Singh , E. Valle , J. McEnaney , S. F. Bent , M. Rønning and T. F. Jaramillo , *Catalysts*, 2021, **11** , 143 .
44. Q. Zhou , Z. Wang , H. Yuan , J. Wang and H. Hu , *Appl. Catal., B*, 2023, **332** , 122750 .
45. Z. Y. Luo , J. J. Li , Y. L. Li , D. J. Wu , L. Zhang , X. Z. Ren , C. X. He , Q. L. Zhang , M. Gu and X. L. Sun , *Adv. Energy Mater.*, 2022, **12** , 2103823.
46. D. C. Han , Z. Y. Luo , Y. Li , N. X. Gao , J. J. Ge , C. P. Liu and W. Xing , *Appl. Surf. Sci.*, 2020, **529** , 147117.
47. Y. Li , Q. F. Gu , B. Johannessen , Z. Zheng , C. Li , Y. T. Luo , Z. Y. Zhang , Q. Zhang , H. I. Fan , W. B. Luo , B. L. Liu , S. X. Dou and H. K. Liu , *Nano Energy*, 2021, **84** , 105898 .
48. Z. Q. Xie , S. L. Yu , X. H. Ma , K. Li , L. Ding , W. T. Wang , D. A. Cullen , H. M. Meyer , H. R. Yu , J. H. Tong , Z. L. Wu and F. Y. Zhang , *Appl. Catal., B*, 2022, **313** , 121458 .
49. X. L. Zhang , P. C. Yu , X. Z. Su , S. J. Hu , L. Shi , Y. H. Wang , P. P. Yang , F. Y. Gao , Z. Z. Wu , L. P. Chi , Y. R. Zheng and M. R. Gao , *Sci. Adv.*, 2023, **9** , eadh2885
50. A. Morozan , H. Johnson , C. Roiron , G. Genay , D. Aldakov , A. Ghedjatti , C. T. Nguyen , P. D. Tran , S. Kinge and V. Artero , *ACS Catal.*, 2020, **10** , 14336 —14348.
51. T. Lim and S. K. Kim , *Chem. Eng. J.*, 2022, **433** , 133681 .
52. P. K. R. Holzapfel , M. Bühler , D. Escalera-López , M. Bierling , F. D. Speck , K. J. J. Mayrhofer , S. Cherevko , C. V. Pham and S. Thiele , *Small*, 2020, **16** , 2003161 .
53. N. Ma and D. Jena , *Phys. Rev. X*, 2014, **4** , 011043 .
54. R. Parsons *Trans. Faraday Soc.*, 1958, **54** , 1053 —1063.

Footnotes

† Electronic supplementary information (ESI) available.

‡ These authors contributed equally to this work.